Fundamental insight into the interaction between a lithium salt and an inorganic filler for ion mobility using a synergic theoretical-experimental approach

Jennifer Bidal [a,b,c,d], Christine Cézard [b,d], Benjamin Bouvier [b,d], Caroline Hadad [b,d], Albert Nguyen Van Nhien [b,d], Matthieu Becuwe [a,c,d,*]

[a] *Laboratoire de Réactivité et Chimie des Solides, UMR 7314 CNRS, Université de Picardie Jules Verne, 33 rue Saint-leu, 80039 Amiens, France*
[b] *Laboratoire de Glycochimie, des Antimicrobiens et des Agroressources, UMR 7378 CNRS, Université de Picardie Jules Verne, 33 rue Saint-leu, 80039 Amiens, France*
[c] *Réseau sur le Stockage Electrochimique de l'Energie (RS2E), France*
[d] *Institut de Chimie de Picardie FR CNRS 3085, 80039 Amiens, France*

GRAPHICAL ABSTRACT
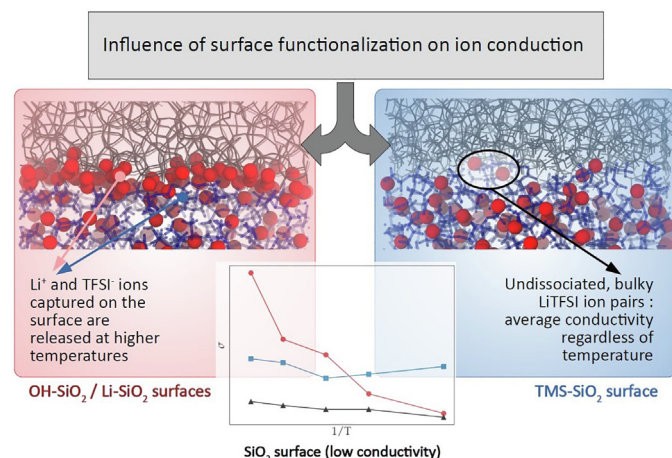
ARTICLE INFO

ABSTRACT

The present paper aims at providing a fundamental insight into the interaction between a lithium salt and an inorganic filler in a perspective of lithium mobility. Through a synergistic approach, coupling experimental results and molecular dynamics simulations, the influence of the surface chemical state of the nanosilica Stöber-type on the dissociation of LiTFSI and its impact on the lithium conduction properties are studied. For this purpose, the surface modification of silica nanoparticles was performed by different methods such as calcination, lithiation and capping with organosilane. The impact of the surface modification on the dissociation of the lithium salt is further investigated by electrochemical impedance spectroscopy after impregnation of the material with a defined amount of lithium salt. The combined experimental and *in silico* analyses of the results, performed for the first time on such systems, allow a

---

* Corresponding author at: Laboratoire de Réactivité et Chimie des Solides, UMR 7314 CNRS, Université de Picardie Jules Verne, 33 rue Saint-leu, 80039 Amiens, France.
 E-mail address: matthieu.becuwe@u-picardie.fr (M. Becuwe).

Molecular dynamic

detailed understanding of the interaction between the salt and the support and should prove itself useful for the future design of hybrid polymer electrolytes in new generation batteries.

1. Introduction

The field of electrochemical energy storage (especially metal-ion batteries) is currently undergoing rapid change due to the massive electrification of our daily life and the drastic decrease of the use of fossil fuels for our mobility. As a result, the demand for increasingly efficient and safer electrical energy storage systems is exponentially growing. To meet this demand, new technologies beyond classical batteries need to be developed to limit price fluctuation and avoid raw material restrictions [1]. While new chemistries involving diverse ions (Na^+, K^+, Ca^{2+}, Mg^{2+},...and even anions) [2–4], sulfur [5,6] or organic-based compounds [7,8] are currently under intense scrutiny, the next generation of batteries is likely to be all-solid since the use of a solid electrolyte can significantly increase the energy density (through bipolar stacking and use of metal anode) but also make the batteries safer [9,10].

The switch to such a technology implies many changes and above all new challenges to overcome such as interfaces management, volume variation control during use and recycling of these batteries at the end of their life. In this context, all attention is focused on the electrolyte, which can be of different chemical natures like inorganic, organic (molecular or polymer) or even hybrid. Each family has its specific advantages, such as the high conductivity of inorganic compounds or the excellent flexibility and processing of polymers, but to date, the perfect electrolyte, combining all the required criteria like good conductivity, broad electrochemical stability, sufficient transport, relatively low cost, etc., has not yet been found. In addition, there are increasing constraints on the availability of raw materials and the recycling of electrolytes, which are more complex for all-solid systems, especially those obtained by sintering. Most probably, as it is currently the case for vehicles, the trend is to progressively evolve from pure inorganic-based electrolyte to hybrid material with different proportions of earth-abundant elements. In this sense, different approaches can be used to design a hybrid electrolyte, such as tethered organic charge carrier [11–14], ionic liquid confinement [15,16], metal-organic framework [17,18] or simply by introducing an inorganic charge, used as filler, into a polymer (CPE, Composite Polymer Electrolyte) [19–21]. The latter represents the most widely used type of hybrid electrolyte.

The main fillers used are ceramic particles of nanometric oxides such as Al_2O_3, SiO_2, ZrO_2, and TiO_2. These fillers do not participate directly in ionic transport but act as "solid plasticizers". They reduce the crystallinity and glass transition temperature of the polymer [22] and could kinetically inhibit the crystallization of the PEO matrix through Lewis acid/base interactions between the surface groups of the ceramic fillers and the polymer segments as well as the lithium salt anion. Since the interface between the inert fillers and the polymer matrix plays a role in improving Li^+ ion conduction, particle size and specific surface area are, therefore, important factors for this improvement [23,24]. In addition to the size of the "inert" ceramic particles, the concentration of the nanoparticles is considered as a second key factor impacting the ionic conductivity of composite electrolyte and can be explained by the cooperation of several factors [23,25]: (i) the decrease of the glass transition temperature with the addition of fine ceramic particles; (ii) the formation of crystallites from the ceramic particles, acting as nucleation centers; (iii) the formation of amorphous phases in the polymer electrolyte, assisted by the inorganic fillers; and (iv) the formation of a new kinetic pathway through the interphase of the polymer matrix and the inert ceramic fillers [22]. Lastly, the surface chemistry of inorganic fillers is also a factor impacting the performance of CPEs. For instance, it has been shown that the more acidic surface of TiO_2 particles allows CPEs to acquire a higher ion transfer number than in the case of Al_2O_3 [21]. SiO_2 is also known to further stabilize the charge-polymer interface due to the hydroxyl groups, responsible for many chemical and physical interactions [26].

In hybrid polymer electrolytes (lithium salt, polymer and inorganic fillers), it is always difficult to estimate which chemical species and which parameters affect and control ion mobility and also how each component interacts together and concomitantly. Thus, a complete understanding of such a system is quite difficult and requires a thorough understanding of the bilateral interactions before the complete ion mobility scheme can be modeled. The present study is the first in a series dedicated to this objective. To the best of our knowledge, lithium ion conduction in lithium salt-filler material has not yet been studied without any other component. To investigate this fundamental question, we propose here a dual experimental-theoretical study focusing on the fillers-salt couple and more specifically on how the surface chemistry of the filler affects the lithium mobility. To this purpose, silica nanoparticles (synthesized using the modified Stöber method) in association with lithium bis(trifluoromethanesulfonyl)imide salt (LiTFSI) have been selected for this study. In order to see clearly the influence of the surface-lithium salt interaction on the conduction properties, the quantity of LiTFSI was intentionally chosen as low (resulting in deliberately low conductivity values) but is perfectly justified to avoid any masking effect of the lithium salt on the conductivity. Different modifications of the SiO_2 surface were carried out, like suppression of hydroxyl groups, surface lithiation and even surface-capping with an organosilane derivative to increase lipophilic interaction.

2. Results and discussion

2.1. Characterization of the synthesized silica NPs (OH-SiO$_2$)

In accordance with the literature [34], infrared spectroscopy of fully hydroxylated silica nanoparticles displays a large and intense band at 3670 cm^{-1} corresponding to free Si-OH groups (Fig. 1a). The size distribution for diameters measured on a sample of 300 nanoparticles was between 40 and 45 nm (mean: 44 nm, standard deviation: 4). The silica nanoparticles were found to be spherical and their size was homogeneously distributed in the sample (Fig. 1b). Subsequently, nitrogen adsorption and desorption isotherms (Fig. 1c) were performed to evaluate the specific surface of the nanoparticles using the equation determined by Brunauer, Emmett and Teller (BET method) [35]. The BET specific surface measured for NPs of size 40–45 nm in diameter was 64 m^2/g. According to the literature, the shape obtained corresponds to type IV to which a hysteresis (type H1) is added [36]. The shape of these isotherms, characteristic of the texture of a material, is usually found in mesoporous solids.
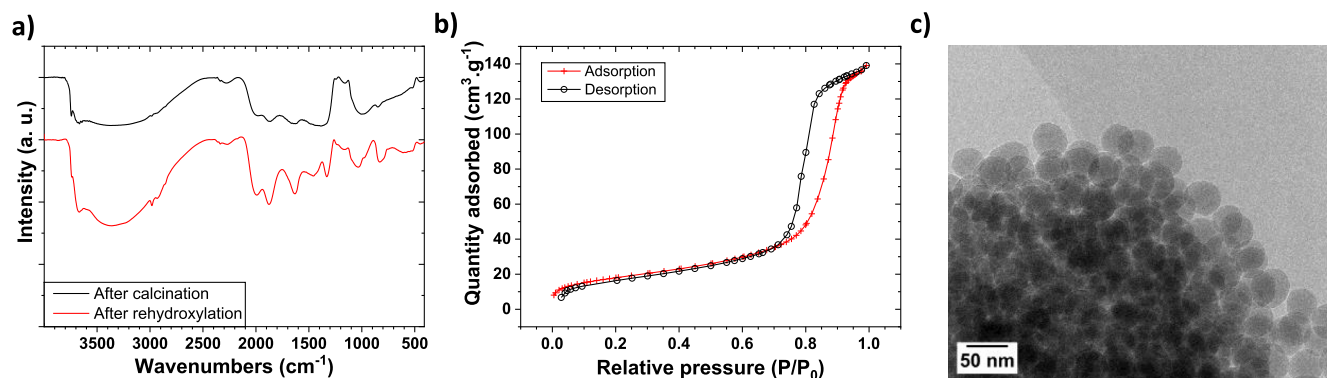
Fig. 1. (a) FTIR spectroscopy in diffuse reflectance mode of OH-SiO$_2$ nanoparticles of diameter 40–45 nm. (b) Bright field TEM image of silica nanoparticles. Size distribution measured on a sample of 300 OH-SiO$_2$ nanoparticles are available in ESI Fig. S1. (c) Nitrogen adsorption (red) and desorption (black) isotherms of synthesized OH-SiO$_2$ nanoparticles of diameter 40–45 nm.

2.2. Surface modifications of hydroxylated SiO$_2$ NP (OH-SiO$_2$)

Several surface modifications were performed on *OH-SiO$_2$* NPs such as lithiation (Li-SiO$_2$), calcination to give hydroxyl-free silica (SiO$_2$), and surface capping with a hydrophobic molecule (MS-SiO$_2$). These modifications were performed in order to probe the impact of the surface state on the ionic conductivity within these samples (Fig. 2).

The modified nanoparticles were first analyzed by FTIR spectroscopy in diffuse reflectance mode to only observe the surface evolution (Fig. 3). For the unmodified (OH-SiO$_2$) and modified NPs (calcinated SiO$_2$, MS-SiO$_2$ and Li-SiO$_2$), a broad band of combination Si-O-Si at 1860 cm^{-1}, a broad band of asymmetric vibrations Si-O-Si between 1000 and 1150 cm^{-1}, a low intensity band at 790 cm^{-1} representing the cyclic structure of SiO$_4$ tetrahedra (siloxane rings) and a band at 515 cm^{-1} attributed to δO-Si-O deformation vibrations were observed, in agreement with the literature [37–40].

Specifically, the removal of labile protons (which can impact the lithium conduction mechanism) was achieved by coating the NPs surface with HMDS reagent under inert conditions (Fig. 3, red curve). In this case, an intense and shifted absorption band at 2963 cm^{-1} attributed to the alkyl groups of the trimethylsilyl moiety (TMS) is observed. The disappearance of the absorption band at 3740 cm^{-1}, corresponding to the stretching vibrations of the iso-
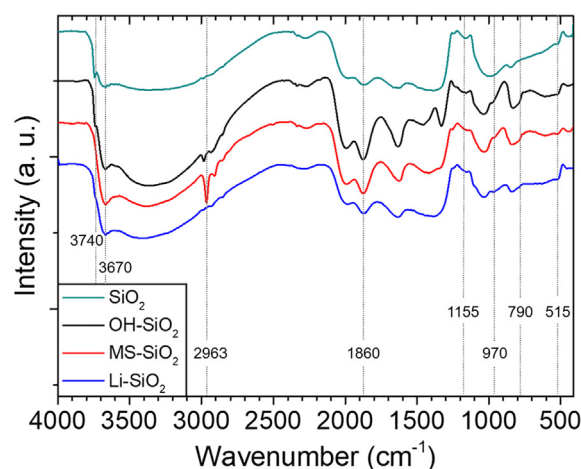

Fig. 3. FTIR spectra of OH-SiO$_2$ nanoparticles (black curve) and surface-modified silica nanoparticles through calcination (SiO$_2$, green curve), methyl-silane capping (MS-SiO$_2$, red curve) and surface lithiation (Li-SiO$_2$, blue curve).

lated Si-OH groups, testifies in favour of the existence of a covalent bond linking the TMS group to the surface OH groups through a Si-O-Si bond. In addition, surface lithiation was performed to study both the influence of lithium addition on the ionic conductivity
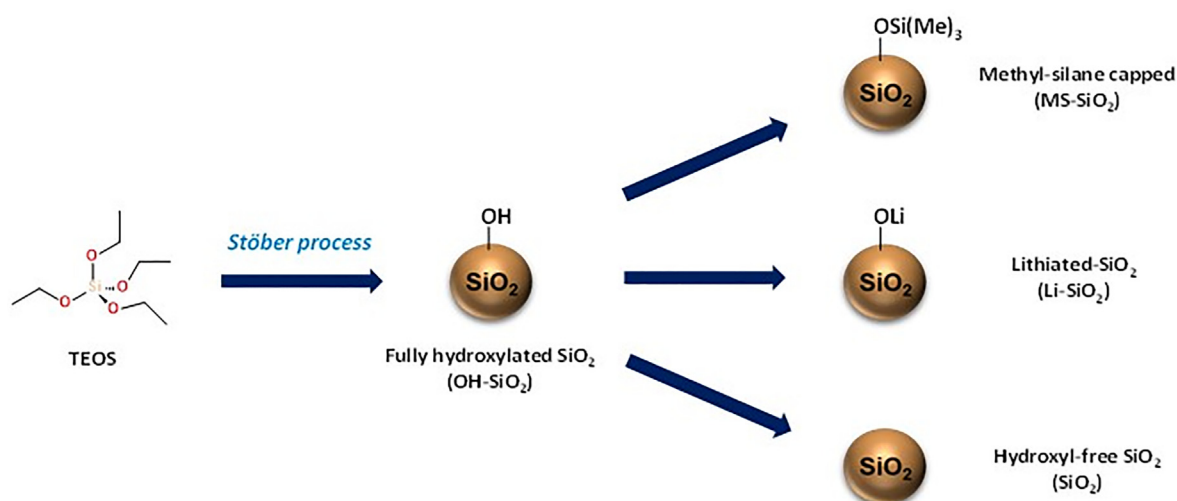

Fig. 2. Surface modifications of hydroxylated SiO$_2$ NPs (OH-SiO$_2$) by surface capping with HMDS (MS-SiO$_2$), Lithiation (Li-SiO$_2$) and hydroxyl-free (SiO$_2$).
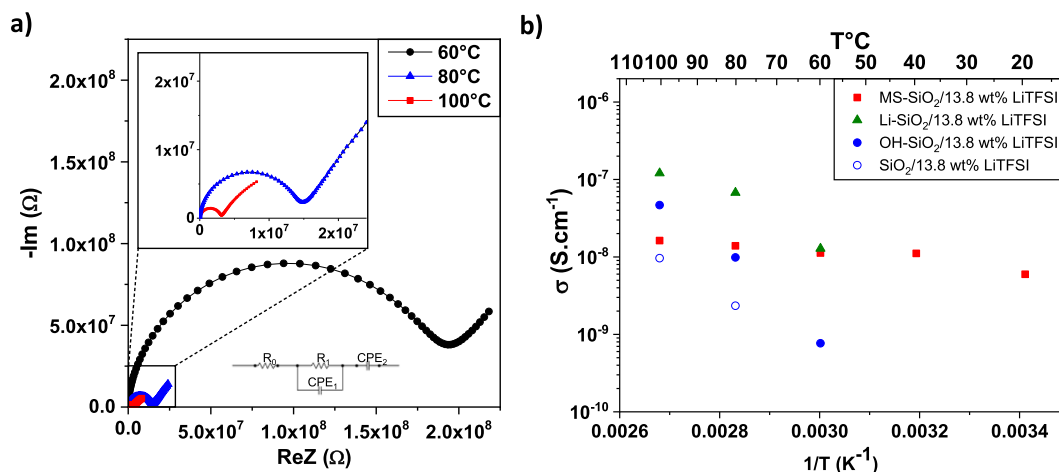
Fig. 4. a) Nyquist diagrams performed at 60 °C, 80 °C, 100 °C of OH-SiO$_2$/13.8 wt% in a blocking electrode/solid electrolyte/blocking electrode system and corresponding equivalent circuit. Nyquist diagrams for other samples are available in SI (Figure S3). b) Temperature dependencies of the ionic conductivity of MS-SiO$_2$, Li-SiO$_2$, OH-SiO$_2$ and SiO$_2$/13.8 wt% LiTFSI, measured between 20 °C and 100 °C.

as well as the role of labile protons (Fig. 3, blue curve). The decrease of the Si-OH absorption band of the isolated silanols at 3740 cm^{-1} attests to an at least partial lithiation of the surface silanols. Finally, the FTIR spectrum analysis of calcined silica NPs (Fig. 3, green curve) reveals the increase in intensity of the absorption band of the isolated Si-OH groups at 3740 cm^{-1}. In accordance with the literature, these groups were formed by the dehydroxylation of silanols involved in hydrogen bonds (with water molecules or vicinal silanol groups) [34]. Conversely, after rehydroxylation (black curve, OH-SiO$_2$) the absorption of the isolated Si-OHs loses intensity to the detriment of silanols linked with hydrogen bonds, whose absorption band gains intensity at 3670 cm^{-1}. Finally, the absorption band located at 970 cm^{-1}, identified as the δSi-OH deformation vibration, is absent from the spectrum of calcined NPs. This information attests to the presence of siloxane bridges. Indeed, the literature testifies to the formation of these bridges from 400 °C, by the thermal dehydration reaction during which two neighbouring silanols condense into a siloxane bridge [34]. At 500 °C, we thus observe at the surface of the nanoparticles a decrease in the Si-OH groups linked by hydrogen bonds, in parallel with an increase in the isolated silanol groups as well as an increase in siloxane bridges.

2.3. Ionic conductivity measurements of unmodified and modified silica NPs

To prepare ionic conductivity measurements by Electrochemical Impedance Spectroscopy (EIS), 13.8 wt% of LiTFSI was mixed with an aqueous suspension containing OH-SiO$_2$ or Li-SiO$_2$, in order to add mobile lithium ions into the material. On the other hand, MS-SiO$_2$ was suspended in acetonitrile due to its hydrophobic surface; the calcined SiO$_2$ sample was similarly handled to prevent the rehydratation of its calcined surface. This relatively low proportion of LiTFSI was chosen intentionally to allow the measurement of the ionic conductivities of the materials (above the detection limit of the measuring devices) while not making the conductivity of LiTFSI interfere with the conductivity values of the studied samples. This fact is important since the goal of this study is to clearly observe and understand the contribution of the surface on the conduction properties.

All samples were transformed into powder, then dried under vacuum at 110 °C overnight before being transferred to a glove box under argon atmosphere. The solid electrolyte obtained did not degrade under air; however, it becomes more hygroscopic as

an increasing amount of LiTFSI is added. This is why a particular attention was paid to avoid any contact with water and moisture during the transfer, at the risk of distorting the conductivity results with the presence of water traces [14].

The ionic conductivity of SiO$_2$/13.8 wt% LiTFSI mixtures of unmodified and modified SiO$_2$ NPs were then studied by EIS at different temperatures (Fig. 4). Initially, the EIS results were plotted in a complex plane in the same way as the OH-SiO$_2$/13.8 wt% LiTFSI sample below (Fig. 4a). All samples have the same appearance: at high frequencies, a semicircle can be seen on each Nyquist plot. At lower frequencies, there is a straight line due to a capacitive effect characteristic of ion blocking electrodes. The line is not completely vertical due to the surface roughness and porosity of the pellets. An appropriate equivalent circuit (Fig. 4a, inset) was used to extract the values corresponding to the resistance of the R1 electrolytes. The ionic conductivity is then calculated for each temperature from the expressions proposed by Ingram et al. [41]. The temperature dependence of the ionic conductivity for X-SiO$_2$/13.8 wt% LiTFSI is shown in Fig. 4b. The conductivity of each sample was calculated from 20 °C to 100 °C. No decomposition or phase transition was observed in this temperature range, as shown by the linear increase in conductivity with temperature for all samples.

Depending on the surface treatment, different behaviours have been observed. The ionic conductivity of OH-SiO$_2$ is very low, below 60 °C, therefore it could only be measured from 60 °C to 100 °C (8.0×10^{-10} and 4.5×10^{-8} S.cm^{-1} respectively). After calcination at 500 °C, the ionic conductivity of SiO$_2$ could only be recorded from 80 °C to 100 °C, respectively 1.5×10^{-9} to 1.0×10^{-8} S.cm^{-1}. The decrease in conductivity can be explained by the increase in the number of siloxane bridges at the expense of isolated Si-OH groups and silanols engaged in hydrogen bonds. Contrary to Si-O-Si bridges, free surface silanols seem to promote conductivity through interactions and complexations of the lithium cation with oxygen atoms. Thus, the –OH groups located on the silica surface are involved in ionic conduction.

The coating of the nanoparticle surface with HMDS (MS-SiO$_2$) was performed to evaluate the role of the labile proton in the conductivity. In the case of MS-SiO$_2$, the conductivity is relatively stable between 20 °C and 100 °C which is quite surprising. These measurements suggest an absence of interaction between the surface and the whole lithium salt, thus inducing a low conductivity (no dissociation) and independent of temperature (no interaction with the surface) even if the ionic conductivities of OH-SiO$_2$ and

MS-SiO$_2$ are comparable at 80 °C. Therefore, although labile protons have been removed, ion conduction is still allowed, demonstrating that labile protons are not involved in the conductivity. On the other hand, the ionic conductivity within Li-SiO$_2$ at 60 °C is one decade higher than that of OH-SiO$_2$; this increase is directly attributed to the presence of additional lithium cations on the surface of the Li-SiO$_2$ material and borne by silanolate groups. Nevertheless, the ionic conductivities of the lithiated and hydroxylated NPs can be measured only at 60 °C and above. This confirms that the trimethylsilane fragment and TFSI interaction releases the lithium cation and thus improves the conduction at lower temperatures. Surface modifications of silica nanoparticles have shown that oxygen atoms participate in conduction while labile protons are not responsible.

2.4. Understanding evolution of the conductivity using molecular dynamics simulations

200 ns of molecular dynamics simulations were performed for each of the silica NPs-LiTFSI systems featuring OH-SiO$_2$, OH-SiO$_2$/Li-SiO$_2$(9%), Li-SiO$_2$, MS-SiO$_2$ or SiO$_2$ surfaces at various temperatures (250 K, 300 K, 350 K, 400 K and 450 K). We then characterized the effects of the distinct silica surface states using the radial distribution functions (RDF) of ions relative to the surface and the ionic number density profiles perpendicular to the surface.

2.4.1. Structuration of LiTFSI around the silica surfaces.

Fig. 5 presents the RDF of the Li$^+$ and TFSI$^-$ ions relative to the silica surfaces at 350 K. It is clear that the surfaces possessing silanol oxygens do not behave the same in presence of LiTFSI than those that do not. For the surfaces bearing silanols, the first peak, sharp and well defined, is located at a distance of 0.2 nm of the silanol oxygens for Li$^+$ and 0.3 nm for TFSI$^-$; for the latter, the second peak around 0.55 nm is also remarkably apparent. This indicates a medium-range structuration of the ionic atmosphere due to strong interactions with the surface. On the other hand, the HDMS and calcinated surface feature monotonous RDFs for both ions, devoid of any peaks, which is indicative of high ionic mobility caused by very weak ion-surface interactions.

We now examine the number density profiles for both ions along the axis perpendicular to the silica surface (Fig. 6). The density is negligible inside the silica slab (where the ingress of ions is

almost never observed) and has a relatively constant value far away from the surface which corresponds to the density of bulk LiTFSI. Near to the surface, interactions with the silica may result in excess of ionic densities which manifest as peaks. Because amorphous silica surfaces are slightly irregular, these peaks can be split into several irregular sub-peaks; however, the resolution still allows to see a distinct alternance of cationic and anionic layers. These observations are consistent with published results obtained for other surfaces and/or ionic liquids [42–44]. Again, it is apparent that the surfaces bearing silanol oxygens interact differently with ions than those without. As expected, Li-SiO$_2$ shows the highest concentration of Li$^+$ ions on its surface, with the TFSI$^-$ ions relegated to the second layer. Li$^+$ also markedly interacts with the OH-SiO$_2$ surface, although the first Li$^+$ layer is a bit more distant from the surface. On the contrary, for MS-SiO$_2$ and calcinated surfaces the first peak is much further away, behind the first layer of anions which become the closest ions to the surface. While this effect could be ascribed purely to steric hindrance in MS-SiO$_2$ (due to the bulky -(CH$_3$)$_3$ groups), its occurrence for the calcinated surface indicates other causes. Comparatively, the layering behaviors of TFSI$^-$ anions around all silica slabs are quite similar (considering the fact that the MS-SiO$_2$ surface is broader), even though these anions represent the first layer for calcinated and MS-SiO$_2$ systems and the second layer for the rest.

Anta et al. argue that the number of TFSI$^-$ ions coordinated to Li$^+$ governs the conducting properties of the electrolyte [45]. In surfaces with silanol oxygens (whether protonated or not), the interfacial Li$^+$ ions interact with the silanol functions and are thus less bound to their TFSI$^-$ counterions than in pure LiTFSI, as indicated by the RDFs between Li$^+$ and TFSI$^-$ presented on Fig. 7. While the RDF in bulk LiTFSI (i.e., far from the surface) is not affected by the surface type, differences near the surface are profound: for MS-SiO$_2$ and calcinated silicas, LiTFSI g(r) feature marked a first and a second peaks comparable to those found in the bulk, showing that the Li$^+$/TFSI$^-$ ion pair is not dissociated by the presence of the surface groups; conversely, silanolated silica surfaces compete with TFSI$^-$ for interacting with Li$^+$ and thus at least partially dissociate the Li$^+$/TFSI$^-$ ion pairs, which translates on the RDF plots as weaker peaks with no resemblance to the bulk.

2.4.2. Conductivity and its origins.

Figures S4a-e show the RDFs for the extreme temperatures of our simulations, i.e. 250 K and 450 K. The locations of the different
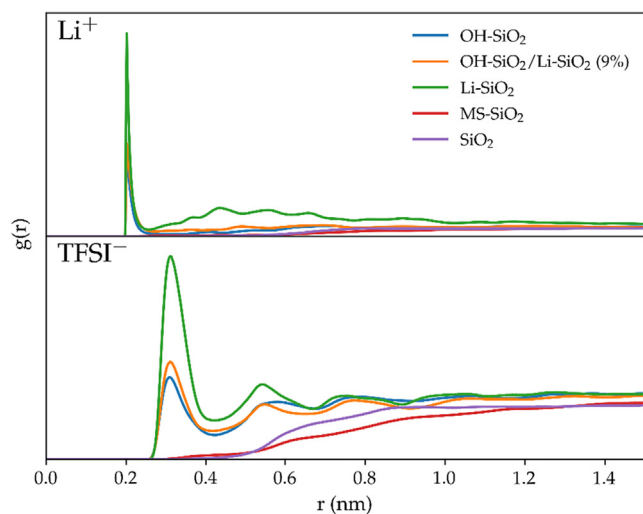

Fig. 5. Radial distribution functions at 350 K between surface atoms and Li$^+$/TFSI$^-$ ions. The reference surface atoms are silanol oxygens for the OH-SiO$_2$ and Li-SiO$_2$ surfaces, carbon atoms for MS-SiO$_2$ and silicon atoms for SiO$_2$.
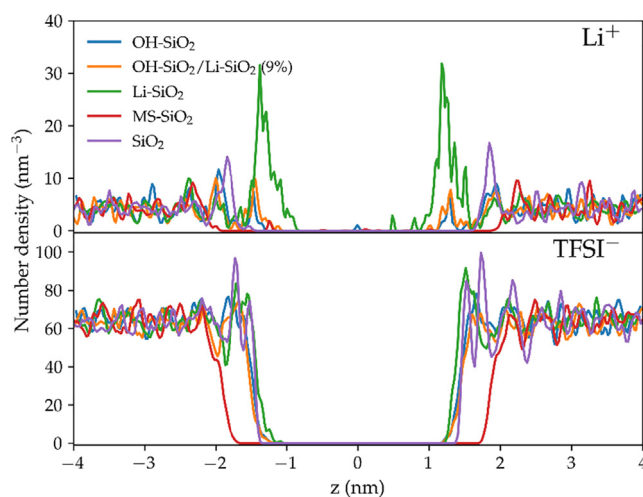

Fig. 6. Number density profiles of Li$^+$ and TFSI$^-$ at 350 K, along the axis perpendicular to the silica surface. The zero-density region of the curves corresponds to the position of the silica slab.
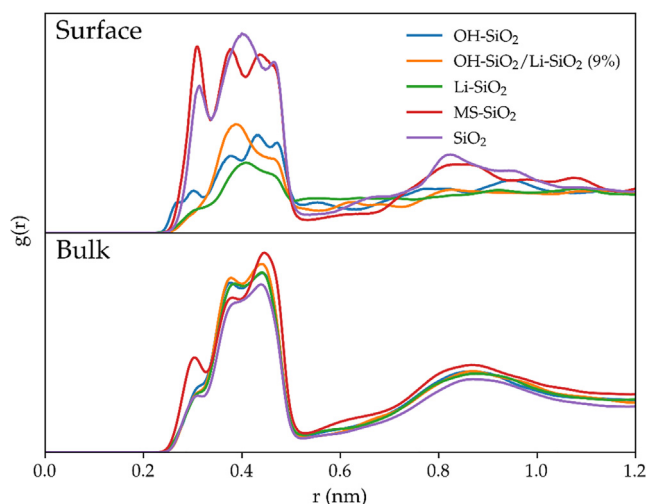
Fig. 7. Radial distribution functions at 350 K between a Li cation and the nitrogen atom of the TFSI anion, obtained in the vicinity of the silica surface and in bulk solvent.

peaks are not modified: they only differ by their heights and widths from their counterparts at 350 K. Indeed, the thermal energy injected into the system by the rise of temperatures is sufficient to lower or break the interactions of the ions with the surface: the ions thus become more mobile, which tends to increase the conductivity. As shown by the 9%-lithiated surface, this effect appears proportional to the surface's degree of lithiation. The number density profiles at 250 K and 450 K (Figures S5a-y) paint a similar picture: at higher temperatures, the layering effect is less pronounced (especially for TFSI$^-$). Sets of radial distribution functions and number density profiles for all systems at extreme temperatures (250 and 450 K) can be found in Supplementary Information. From the molecular dynamics simulations at different temperatures, we compute the theoretical conductivities of our systems using the Einstein-Helfand model [46] (Fig. 8) and compare them to their experimental counterparts on Fig. 4b. Theory and experiment agree that the ionic conductivity for the MS-SiO$_2$ surface is only slightly affected by temperature changes. As previ-

ously stated, the RDF and number density profiles clearly indicate that there is no strong interaction between the silica surface and the salt in this system. Raising the temperature thus only increases the thermal motion of the electrolyte ions, only causing a small elevation of the total conductivity. Ionic conductivities measured for the MS-SiO$_2$/LiTFSI system also show almost no temperature dependence, just like in our simulations; considering how little the surface affects the Li$^+$/TFSI$^-$ ion pairs (see above), we expect these conductivities to be close to those of bulk LiTFSI. Conversely, for all other systems, there is a marked correlation between conductivity and temperature, observed both in experimental measures and molecular dynamics results. The substantial augmentation of conductivity observed upon temperature elevation is not only linked to the increase of thermal motion of Li$^+$/TFSI$^-$, but is a consequence of the detachment of Li$^+$ cations from the surface via the thermal weakening of electrostatic interactions with the silanol oxygens. The resulting increase in the mobility of these cations, clearly indicated by the broadening and the shortening of the first peak of the Li-O$_{silanol}$ radial distribution function (Fig. 5) upon temperature increase, contributes positively to conductivity via the facilitated diffusion of charges.

In our model, conductivity thus appears as a tradeoff mediated by the relative strengths of the Li$^+$/O$_{silanol}$ and Li$^+$/TFSI$^-$ interactions. Once dissociated from its bulky TFSI$^-$ counterion by interaction with the silanols, Li$^+$ ions can diffuse efficiently due to their small radii, enhancing conductivity; however, at lower temperatures, they become "trapped" by the silanols and conductivity falls. Conversely, in the absence of strong interactions with the surface, the Li$^+$/TFSI$^-$ ion pair endures regardless of temperature, but its large radius strongly limits its diffusive capabilities. The good match between experimental and theoretical results proves the dominance of this model over other possible sources of conductivity that are not included in our simulations: for instance, charge or electron transfer phenomena which require a quantum mechanical description are incompatible with long simulation timescales.

In the future, it would be interesting to study the interaction between LiTFSI and small POE oligomers and polymers using this synergistic approach, and then build a larger model to finely understand ion mobility and study how composite structure and composition affect ion mobility and transport.

3. Conclusions

Through this study, the origin of the conductivity of the LiTFSI in close interaction with a inorganic filler was scrutinized. By combining experimental measurements and *in silico* models, we were able to unambiguously ascribe differences in conductivity to the degree of dissociation of the Li$^+$/TFSI$^-$ ion pair, which is itself modulated by interactions with the functionalized silica surface. It is now clear that the functionalization of oxygen atoms on the silica NPs plays a critical role in conduction properties. The replacement of labile protons with lithium induces a conductivity jump of one decade, revealing that conductivity is mediated by the relative strengths of the Li$^+$/O$_{silanol}$ and Li$^+$/TFSI$^-$ interactions. Conversely, by hindering the dissociation of LiTFSI, the grafting of hydrophobic methylsilane fragments prevents the interaction of Li with the silica surface and leads to a temperature-independent conductivity curve. Finally, the computational model employed here has been validated by its good agreement with the experimental results. It would be interesting to extend this approach to study other interactions such as lithium salt with different PEO-based oligomers/polymers or to predict the surface functionalization needed to optimize conductivity at a given temperature. These aspects could thus serve as a basis for building a larger model that could prove useful as a preliminary step in the future design of hybrid electrolytes in next generation batteries.
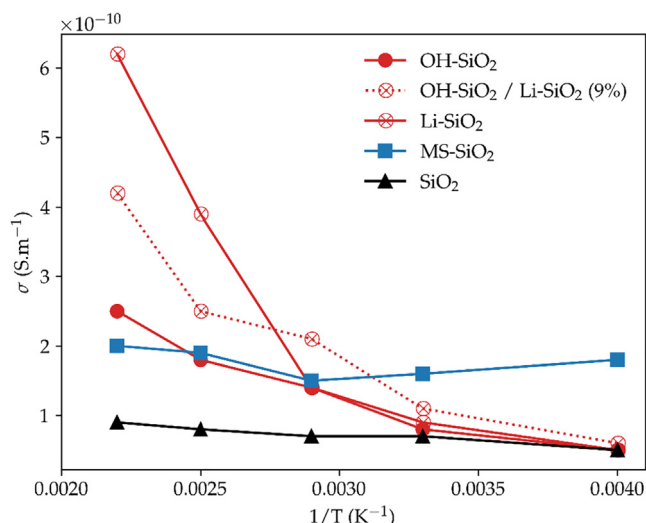

Fig. 8. Static conductivities obtained using Einstein-Helfand fitting.

4. Experimental section

4.1. Reagents and Chemicals

Chemicals and solvents such as tetraethylorthosilicate (TEOS), ammonia solution (30 wt%), lithium bis(trifluoromethylsulfonyl)imide salt (LiTFSI), 1,1,1,3,3,3-hexamethyldisilazane (HMDS), lithium hydroxide and ethanol were purchased form Sigma Aldrich as reagent grade or better and used as received. Toluene was pre-dried over sodium and distilled prior to use. HMDS was purchased dried and was stored under argon in a glovebox.

4.2. Instrumentation

N_2-adsorption isotherms were measured at liquid nitrogen temperature with a Micrometric ASAP 2020 porosimeter. Prior to analysis, the sample surface was outgassed at 120 °C for 3 h under vacuum (ca. 1 mm Hg). The Brunauer-Emmett-Edward (BET) surface area was calculated from the adsorption part of the isotherm between $0.03 < P/P_0 < 0.3$ using a multi-point method. The different synthesized materials were characterized by FTIR spectra in diffuse reflectance mode (DRIFT) using a Nicolet iS10 FTIR spectrometer from Thermo Scientific. The spectra were acquired at room temperature over a range of 4000–400 cm^{-1} with a resolution of 8 cm^{-1}. Electrochemical impedance spectroscopy (EIS) measurements were realized with an MTZ-35 frequency response analyzer (BioLogic Company) coupled with an Intermediate Temperature System (ITS) controlling the sample temperature by Peltier effect. The different synthesized materials were cold-pressed into pellets of 10 mm diameter under a pressure of 5 tons with around 70 mg of powder per pellet. Thicknesses of about 0.60 mm were obtained. The pellets were sandwiched between two aluminium foils (sheet thickness: 0.006 mm) enhancing the electrical contacts between the pellet surface and the controlled environment sample holder (CESH) gold disks. The combined aluminium foil and gold disk ensured an ion blocking electrode. The electrolyte pellet was transferred under argon (in a glovebox) into an airtight environment asymmetric CESH to be sandwiched between the two-ion blocking aluminium-gold electrodes. The CESH was then placed in ITS, and AC impedance spectra was recorded in the frequency range from 30 MHz to 0.1 Hz with an excitation signal of 5 mV amplitude and from 20 to 100 °C upon heating and cooling (1 °C·min^{-1}) with a temperature stabilization of 15 min before impedance measurement every 20 °C. Modelling and simulation of the EIS data were performed using an equivalent circuit model described in the discussion section. Quantitative analyses were done using the Zview software (Scribner Associates, Inc.). Conductivity measurements were realized three times (second measurement on the same pellet and one measurement on a new pellet) in order to ensure reproducibility.

4.3. Synthesis of silica nanoparticles

Silica nanoparticles were obtained using the Stöber process, briefly described as follows [27]. A solution of absolute ethanol (500 mL) was mixed to a 30 wt% ammonia solution (38 mL, 0.29 mol) and the mixture was stirred for 1 h at 70 °C. TEOS (15 mL, 67.25 mmol) was then added dropwise. The first nanometric objects were observed after a few minutes, thus forming a translucent colloidal suspension. The solution was stirred for 12 h to completely hydrolyze the Si-precursor. Silica nanoparticles were recovered by centrifugation (8000 rpm) and washed several times with absolute ethanol and distilled water. The inorganic nanoparticles were calcined at 500 °C (5 °C/min heating rate) for 6 h in order to remove residual solvent and organic species remaining on the silica surface. After being cooled to room temperature, silica nanoparticles were hydrated in a concentrated (37%) HCl solution at 100 °C for 12 h. The silica nanoparticles (named OH-SiO_2) were then washed with water by centrifugation until neutral pH and finally dried under vacuum at 100 °C before use.

4.3.1. LiOH modification of silica surface (Li-SiO_2)

Considering the silica specific surface area (64 m^2.g^{-1}) and considering a maximum of two OH per nm^2 at the SiO_2 surface, 3 equivalents of LiOH were added to 1 g of the synthesized OH-SiO_2 suspended in water. The obtained mixture was stirred at room temperature overnight and then washed five times by centrifugation with water. The nanoparticles (Li-SiO_2) were finally recovered after solvent evaporation and dried overnight under vacuum at 100 °C.

4.3.2. Hydrophobic capping of silica nanoparticles (MS-SiO_2)

The synthesized silica nanoparticles OH-SiO_2 (1 g) were dried under vacuum at 100 °C overnight before being suspended in 20 mL of dry toluene. An excess of dried HMDS (1 mL) was added to the suspension and stirred overnight at room temperature under inert condition. The obtained mixture was washed five times by centrifugation with toluene then the resulting powder (MS-SiO_2) was dried under vacuum at 120 °C overnight.

4.3.3. Suppression of silica surface hydroxyl groups (SiO_2)

OH-SiO_2 were calcined at 500 °C (5 °C/min heating rate) overnight in order to remove as many hydroxyl groups of the silica surface as possible. After calcination, the material (SiO_2) was transferred to an Argon-filled glovebox to avoid any adsorption of moisture.

4.4. LiTFSI impregnation

Depending on the LiTFSI weight percentage, a desired amount of LiTFSI dissolved in 20 mL of water (OH-SiO_2 and Li-SiO_2) or anhydrous acetonitrile (SiO_2 and MS-SiO_2) was added under inert atmosphere to the unmodified and modified silica nanoparticles. The suspension was then homogenized by sonication. The solvent was removed by a slow evaporation with vigorous stirring at 70 °C overnight.

4.5. Simulation details

All molecular dynamics simulations were carried out using GROMACS 2018.3 [28]. In a first step, equilibrated structures of the different silica slabs were obtained from NPT simulations at 500 K, which were subsequently used as starting points for stepwise temperature annealing simulations. Equilibrated initial frames for production runs at 250 K, 300 K, 350 K, 400 K and 450 K were thus obtained. Finally, 200 ns production simulations, from which the diffusion and conductivity values were measured, were performed at each of these temperatures for all silica slabs. These simulations used a 2 fs integration timestep; temperature in the NVT ensemble was regulated using a Nose-Hoover thermostat with a time constant of 1.3 fs and separate couplings to the silica slab, cations and anions. All-atom models of silica slabs (surface-capped and calcinated) including geometry and force field parameters were taken from reference [29]. An amorphous surface with 4.7 silanol groups per nm^2 is suited to model medium Stöber silica particles, the surface area being approximately of 4 nm × 4 nm and the slab thickness 2.4 nm. Force field parameters for LiTFSI were taken from references [30,31]; as explained in these works, respective charges of 0.8e and –0.8e for the cation and anion were used. The silica-LiTFSI boxes sizes were in the 4 nm × 4 nm × 8 nm range and the number of salt ion pairs were

calculated to reproduce the experimental LiTFSI bulk density (1.33 g.cm^{-3}). The deprotonated surfaces were obtained by deleting hydrogen atoms from the Si-OH groups and adding chloride counterions. The hydrophobic surface was obtained by replacing the hydrogen atoms of the Si-OH groups by a Si(CH$_3$)$_3$ function, whose parameters were taken from the AMBER99SB force field [32] and the atomic charges obtained using REDserver [33].

CRediT authorship contribution statement

Jennifer Bidal: Investigation. **Christine Cézard:** Formal analysis, Software. **Benjamin Bouvier:** Formal analysis, Software. **Caroline Hadad:** Writing – review & editing. **Albert Nguyen Van Nhien:** Writing – review & editing. **Matthieu Becuwe:** Supervision, Funding acquisition, Project administration.

Declaration of Competing Interest

The authors declare that they have no known competing financial interests or personal relationships that could have appeared to influence the work reported in this paper.

Acknowledgments

Appendix A. Supplementary material

Supplementary data to this article can be found online at https://doi.org/10.1016/j.jcis.2022.06.072.

References

[1] M. Iglesias-Émbil, A. Valero, A. Ortego, M. Villacampa, J. Vilaró, G. Villalba, Raw material use in a battery electric car – a thermodynamic rarity assessment, Resour. Conserv. Recycl. 158 (2020) 104820, https://doi.org/10.1016/j.resconrec.2020.104820.

[2] C. Delmas, Sodium and Sodium-Ion Batteries: 50 Years of Research, Adv. Energy Mater. 8 (2018) 1–9, https://doi.org/10.1002/aenm.201703137.

[3] R. Dominko, J. Bitenc, R. Berthelot, M. Gauthier, G. Pagot, V. Di Noto, Magnesium batteries: Current picture and missing pieces of the puzzle, J. Power Sources 478 (2020) 229027, https://doi.org/10.1016/j.jpowsour.2020.229027.

[4] S. Dong, Z. Li, I.A. Rodríguez-Pérez, H. Jiang, J. Lu, X. Zhang, X. Ji, A novel coronene//Na2Ti3O7 dual-ion battery, Nano Energy 40 (2017) 233–239, https://doi.org/10.1016/j.nanoen.2017.08.022.

[5] G. Cohn, L. Ma, L.A. Archer, A novel non-aqueous aluminum sulfur battery, J. Power Sources 283 (2015) 416–422, https://doi.org/10.1016/j.jpowsour.2015.02.131.

[6] S. Wei, S. Xu, A. Agrawral, S. Choudhury, Y. Lu, Z. Tu, L. Ma, L.A. Archer, A stable room-temperature sodium–sulfur battery, Nat. Commun. 7 (2016) 11722, https://doi.org/10.1038/ncomms11722.

[7] P. Poizot, J. Gaubicher, S. Renault, L. Dubois, Y. Liang, Y. Yao, Opportunities and Challenges for Organic Electrodes in Electrochemical Energy Storage, Chem. Rev. 120 (2020) 6490–6557, https://doi.org/10.1021/acs.chemrev.9b00482.

[8] Y. Lu, J. Chen, Prospects of organic electrode materials for practical lithium batteries, Nat. Rev. Chem. 4 (2020) 127–142.

[9] T. Famprikis, P. Canepa, J.A. Dawson, M.S. Islam, C. Masquelier, Fundamentals of inorganic solid-state electrolytes for batteries, Nat. Mater. 18 (2019) 1278–1291, https://doi.org/10.1038/s41563-019-0431-3.

[10] J. Janek, W.G. Zeier, A solid future for battery development, Nat. Energy 1 (2016) 1–4, https://doi.org/10.1038/nenergy.2016.141.

[11] K.S. Korf, Y. Lu, Y. Kambe, L.A. Archer, Piperidinium tethered nanoparticle-hybrid electrolyte for lithium metal batteries, J. Mater. Chem. A 2 (2014) 11866–11873, https://doi.org/10.1039/c4ta02219j.

[12] S. Delacroix, F. Sauvage, M. Reynaud, M. Deschamps, S. Bruyère, M. Becuwe, D. Postel, J.M. Tarascon, A.N. Van Nhien, SiO2/Ionic Liquid Hybrid Nanoparticles for Solid-State Lithium Ion Conduction, Chem. Mater. 27 (2015) 7926–7933, https://doi.org/10.1021/acs.chemmater.5b02944.

[13] Y. Lu, S.K. Das, S.S. Moganty, L.A. Archer, Ionic Liquid-Nanoparticle Hybrid Electrolytes and their Application in Secondary Lithium-Metal Batteries (2012) 4430–4435. doi:10.1002/adma.201201953.

[14] J. Bidal, M. Becuwe, C. Hadad, B. Fleutot, C. Davoisne, M. Deschamps, B. Porcheron, A.N.V. Nhien, Hybrid Electrolytes Based on Optimized Ionic Liquid Quantity Tethered on ZrO2 Nanoparticles for Solid-State Lithium-Ion Conduction, ACS Appl. Mater. Interfaces 13 (2021) 15159–15167, https://doi.org/10.1021/acsami.0c22422.

[15] X. Chen, B. Put, A. Sagara, K. Gandrud, M. Murata, J.A. Steele, H. Yabe, T. Hantschel, M. Roeffaers, M. Tomiyama, et al., Silica gel solid nanocomposite electrolytes with interfacial conductivity promotion exceeding the bulk Li-ion conductivity of the ionic liquid electrolyte filler, Sci. Adv. 6 (2020) 1–12, https://doi.org/10.1126/sciadv.aav3400.

[16] A. Guyomard-Lack, B. Said, N. Dupré, A. Galarneau, J. Le Bideau, Enhancement of lithium transport by controlling the mesoporosity of silica monoliths filled by ionic liquids, New J. Chem. 40 (2016) 4269–4276, https://doi.org/10.1039/c5nj03318g.

[17] Z. Wang, Z. Wang, L. Yang, H. Wang, Y. Song, L. Han, K. Yang, J. Hu, H. Chen, F. Pan, Boosting interfacial Li+ transport with a MOF-based ionic conductor for solid-state batteries, Nano Energy 49 (2018) 580–587, https://doi.org/10.1016/j.nanoen.2018.04.076.

[18] Z. Wang, R. Tan, H. Wang, L. Yang, J. Hu, H. Chen, F. Pan, A Metal–Organic-Framework-Based Electrolyte with Nanowetted Interfaces for High-Energy-Density Solid-State Lithium Battery, Adv. Mater. 30 (2018) 1–7, https://doi.org/10.1002/adma.201704436.

[19] D. Brandell, A. Liivat, H. Kasemägi, A. Aabloo, J.O. Thomas, Molecular dynamics simulation of the LiPF6·PEO 6 structure, J. Mater. Chem. 15 (2005) 1422–1428, https://doi.org/10.1039/b417232a.

[20] S.K. Das, A.J. Bhattacharyya, Influence of oxide particle network morphology on ion solvation and transport in "soggy Sand" Electrolytes, J. Phys. Chem. B 114 (2010) 6830–6835, https://doi.org/10.1021/jp102548e.

[21] F. Groce, G.B. Appetecchi, L. Persi, B. Scrosati, Nanocomposite polymer electrolytes for lithium batteries, Nature 394 (1998) 455–482, https://doi.org/10.1557/proc-496-511.

[22] Q. Zhang, K. Liu, F. Ding, X. Liu, Recent advances in solid polymer electrolytes for lithium batteries, Nano Res. 10 (2017) 4139–4174, https://doi.org/10.1007/s12274-017-1763-4.

[23] J. Przyluski, M. Siekierski, W. Wieczorek, Effective medium theory in studies of conductivity of composite polymeric electrolytes, Electrochim. Acta 40 (1995) 2101–2108, https://doi.org/10.1016/0013-4686(95)00147-7.

[24] W. Wieczorek, J.R. Stevens, Z. Florjańczyk, Composite polyether based solid electrolytes. The Lewis acid-base approach, Solid State Ionics 85 (1996) 67–72, https://doi.org/10.1016/0167-2738(96)00042-2.

[25] S. Rajendran, T. Uma, Effect of ceramic oxide on PVC-PMMA hybrid polymer electrolytes, Ionics (Kiel). 6 (2000) 288–293, https://doi.org/10.1007/BF02374079.

[26] D. Lin, W. Liu, Y. Liu, H.R. Lee, P.C. Hsu, K. Liu, Y. Cui, High Ionic Conductivity of Composite Solid Polymer Electrolyte via in Situ Synthesis of Monodispersed SiO2 Nanospheres in Poly(ethylene oxide), Nano Lett. 16 (2016) 459–465, https://doi.org/10.1021/acs.nanolett.5b04117.

[27] W. Stöber, A. Fink, E. Bohn, Controlled growth of monodisperse silica spheres in the micron size range, J. Colloid Interface Sci. 26 (1968) 62–69, https://doi.org/10.1016/0021-9797(68)90272-5.

[28] M. James, T. Murtola, R. Schulz, J.C. Smith, B. Hess, E. Lindahl, ScienceDirect GROMACS : High performance molecular simulations through multi-level parallelism from laptops to supercomputers 2 (2015) 19–25, doi:10.1016/j.softx.2015.06.001.

[29] F.S. Emami, V. Puddu, R.J. Berry, V. Varshney, S.V. Patwardhan, C.C. Perry, H. Heinz, Force Field and a Surface Model Database for Silica to Simulate Interfacial Properties in Atomic Resolution, Chem. Mater. 26 (2016) 2647–2658.

[30] S.V. Sambasivarao, O. Acevedo, Development of OPLS-AA force field parameters for 68 unique ionic liquids, J. Chem. Theory Comput. 5 (2009) 1038–1050, https://doi.org/10.1021/ct900009a.

[31] B. Doherty, X. Zhong, S. Gathiaka, B. Li, O. Acevedo, Revisiting OPLS Force Field Parameters for Ionic Liquid Simulations, J. Chem. Theory Comput. 13 (2017) 6131–6135, https://doi.org/10.1021/acs.jctc.7b00520.

[32] V. Hornak, R. Abel, A. Okur, B. Strockbine, A. Roitberg, C. Simmerling, Las instituciones de ciencia y tecnología en los procesos de aprendizaje de la producción agroalimentaria en Argentina, Proteins Struct. Funct. Bioinforma. 65 (2006) 712–725, https://doi.org/10.1002/prot.

[33] E. Vanquelef, S. Simon, G. Marquant, E. Garcia, G. Klimerak, J.C. Delepine, P. Cieplak, F.Y.R.E.D. Dupradeau, Server: A web service for deriving RESP and ESP charges and building force field libraries for new molecules and molecular fragments, Nucl. Acids Res. 39 (2011) 511–517, https://doi.org/10.1093/nar/gkr288.

[34] V. Dugas, Y. Chevalier, Surface hydroxylation and silane grafting on fumed and thermal silica, J. Colloid Interface Sci. 264 (2003) 354–361, https://doi.org/10.1016/S0021-9797(03)00552-6.

[35] S. Brunauer, P.H. Emmett, E. Teller, Adsorption of gases in Multimolecular layers, J. Am. Chem. Soc. 60 (1938) 309–319.

[36] K.S.W. Sing, Adsorption methods for the characterization of porous materials, Adv. Colloid Interface Sci. 76–77 (1998) 3–11, https://doi.org/10.1016/S0001-8686(98)00038-4.

[37] R. Tian, O. Seitz, M. Li, W. Hu, Y.J. Chabal, J. Gao, Infrared characterization of interfacial Si-O bond formation on silanized flat SiO2/Si Surfaces, Langmuir 26 (2010) 4563–4566, https://doi.org/10.1021/la904597c.

[38] H. Alloul, T. Roques-Carmes, J. Toufaily, M. Kassir, M. Pelletier, A. Razafitianamaharavo, T. Hamieh, F. Villiéras, Towards a better description of organosilane grafting onto silica particles using volumetric techniques based on molecular probing, Adsorption 22 (2016) 923–937, https://doi.org/10.1007/s10450-016-9800-2.

[39] V.M. Gun'Ko, M.S. Vedamuthu, G.L. Henderson, J.P. Blitz, Mechanism and kinetics of hexamethyldisilazane reaction with a fumed silica surface, J. Colloid Interface Sci. 228 (2000) 157–170, https://doi.org/10.1006/jcis.2000.6934.

[40] M. Catauro, E. Tranquillo, R. Risoluti, S.V. Ciprioti, Sol-Gel synthesis, spectroscopic and thermal behavior study of SiO2/PEG composites containing different amount of chlorogenic acid, Polymers (Basel) 10 (2018), https://doi.org/10.3390/polym10060682.

[41] B.J. Ingram, B.J. Harder, N.W. Hrabe, T.O. Mason, K.R. Poeppelmeier, Transport and defect mechanisms in cuprous delafossites. 2. CuScO 2 and CuYO2, Chem. Mater. 16 (2004) 5623–5629, https://doi.org/10.1021/cm048982k.

[42] C. Aliaga, C.S. Santos, S. Baldelli, Surface chemistry of room-temperature ionic liquids, Physical Chemistry Chemical Physics 9 (2007), https://doi.org/10.1039/b703574h.

[43] F. Federici Canova, M. Mizukami, T. Imamura, K. Kurihara, A.L. Shluger, Structural stability and polarisation of ionic liquid films on silica surfaces, Phys. Chem. Chem. Phys. 17 (2015) 17661–17669, https://doi.org/10.1039/c5cp02299a.

[44] T. Pal, C. Beck, D. Lessnich, M. Vogel, Effects of Silica Surfaces on the Structure and Dynamics of Room-Temperature Ionic Liquids: A Molecular Dynamics Simulation Study, J. Phys. Chem. C 122 (2018) 624–634, https://doi.org/10.1021/acs.jpcc.7b10567.

[45] J.M. Vicent-Luna, E. Azaceta, S. Hamad, J.M. Ortiz-Roldán, R. Tena-Zaera, S. Calero, J.A. Anta, Molecular Dynamics Analysis of Charge Transport in Ionic-Liquid Electrolytes Containing Added Salt with Mono, Di, and Trivalent Metal Cations, ChemPhysChem 19 (2018) 1665–1673, https://doi.org/10.1002/cphc.201701326.

[46] H. Eugene, C4 journal of experimental and theoretical physics established by K L. Nichols in 1S93 Transport Coefficients from Dissipation in a Canonical Ensemble, Phys. Rev. 119 (1960) 1–9.